Contents lists available at ScienceDirect

Transactions of Nonferrous Metals Society of China

36(2026) 902−916

www.tnmsc.cn

Effects of γ-ray and electron irradiation on microstructural evolution and mechanical properties of SnPb eutectic solder joints

Qi-long GUAN [a], Chun-jin HANG [a,b,*], Wei ZHANG [a], Sheng-li LI [a], Xiao-jiu TANG [a], Dan YU [c], Ying DING [c], Xiu-li WANG [c], Yu-bao ZHANG [d,**]

[a] National Key Laboratory of Precision Welding & Joining of Materials and Structures, Harbin Institute of Technology, Harbin 150006, China;

[b] Zhengzhou Research Institute, Harbin Institute of Technology, Zhengzhou 450046, China;

[c] Beijing Institute of Control Engineering, Beijing 100094, China;

[d] Heilongjiang Institute of Atomic Energy, Harbin 150086, China

Abstract: The effects of γ-ray and electron irradiation on the microstructural evolution and mechanical properties of SnPb eutectic solder joints were investigated. Following electron irradiation, the SnO_2 phase induced by γ-ray irradiation transformed into β-Sn, and the dislocation density in the β-Sn crystal decreased. Moreover, numerous point defect clusters formed in the β-Sn crystal, some of which transformed into an amorphous phase, increasing the amorphous layer thickness. Meanwhile, electron irradiation likewise resulted in rotation of the (220) plane of β-Sn nanograins and reduction of SnO_2 in the β-Sn crystal. Additionally, upon exposure to γ-ray and electron irradiation, the average shear strength of the solder balls was initially increased by 10.10%, followed by a decrease of 3.53% and 4.77%, respectively. The plasticity and the dimple count on the fracture surfaces of the solder joint initially decreased but subsequently increased.

Keywords: combined irradiation; SnPb eutectic solder joints; SnO_2 reduction; irradiation damage; β-Sn nanograin rotation

1 Introduction

Deep space exploration, extending beyond Earth's gravitational domain into the broader solar system, is driven by three principal objectives. The foremost aim is to address fundamental scientific inquiries about the formation and evolution of the solar system, the universe, and the origins of life, thereby establishing a foundational pillar for human space exploration efforts. Secondly, it fosters the advancement of space technology, supporting sustainable development and strengthening our capacity for further space exploration. Thirdly, it propels the growth of fundamental and emerging disciplines and technologies, and consequently drives progress across interconnected scientific domains. With the continuous advancement of space technology, nations worldwide have planned a variety of long-duration and long-distance missions for deep space exploration. During their operational lifetimes, deep space exploration spacecrafts endure harsh space environments characterized by extreme temperatures, intense radiation, as well as large temperature variations. These factors pose substantial risks to spacecraft reliability. Space radiation, which generates γ-rays, high-energy electrons, neutrons, and heavy ions, can result in

Corresponding author: *Chun-jin HANG, Tel: +86-18686868816, E-mail: hangcj@hit.edu.cn;
**Yu-bao ZHANG, Tel: +86-15045037816, E-mail: zyb-bob@sohu.com

https://doi.org/10.1016/S1003-6326(25)67005-1
Received 28 May 2024; accepted 25 March 2025

cumulative radiation damage to electronic components and solder joints over prolonged operational periods and vast distances, eventually causing performance degradation or failure of electronic systems.

The quality of solder joints is vital to ensuring the reliability, performance, and longevity of electronic devices, as they serve as both mechanical and electrical connections to the printed circuit board (PCB). Moreover, statistics data indicate that assembly issues account for 70% of electronic device failures, with solder joint failures representing a substantial contributing factor. Radiation shielding enclosures are commonly used to protect onboard electronics and solder joints from space radiation. However, this method significantly increases weight, lowers the payload-to-mass ratio, raises launch costs, and contradicts the goals of miniaturization and lightweight design essential for deep space exploration. Additionally, it fails to protect exposed components and solder joints, including those found in solar arrays.

As the aerospace industry is exempt from RoHS and WEEE directives, Pb-containing solder alloys are extensively used in spacecraft manufacturing due to their superior wetting characteristics and low-temperature performance. Current research on solder joint reliability has predominantly focused on conditions including thermal aging [1−3], thermal shock [4,5], as well as electromigration [6,7]. Nevertheless, the effects of irradiation on the microstructural evolution and mechanical properties of solder joints have not been thoroughly investigated. Specifically, merely a limited number of investigations have examined the influence of γ-ray irradiation on Sn3Ag0.5Cu (SAC305) [8,9], SnPb eutectic [10] and SnPbSb/Cu [11,12] solder joints. In our previous studies [13,14], the nanoscale mechanisms driving the microstructural evolution of SAC305 and SnPb eutectic solder joints under γ-ray irradiation for up to 200 h were comprehensively elucidated. The findings demonstrated the micro-structural damage mechanisms at both micron and nanometer scales, as well as oxidation processes induced by γ-ray irradiation. Moreover, since solder joints in onboard electronic devices are exposed to both γ-rays and a wide range of cosmic radiation, their long-term reliability is significantly challenged by these factors. To more accurately simulate the space environment, γ-rays from a ^{60}Co source with an average energy of 1.25 MeV, along with 1.2 MeV electrons, were employed to co-irradiate SnPb eutectic solder joints. The mechanisms of microstructural evolution and the alterations in the mechanical properties of SnPb eutectic solder joints under γ-ray and electron irradiation were examined.

2 Experimental

2.1 Specimen preparation

The focused ion beam (FIB) specimen for the transmission electron microscopy (TEM) observation was prepared by TESCAN AMBER from a SnPb eutectic solder joint (63Sn37Pb, in wt.%) cross-section, as demonstrated in Figs. 1(a−c). Besides, the Cu pad on the PCB was coated with electrolytic NiAu finishing, and the diameter of the surface mounted device (SMD) aperture forming the pad/solder interface was 300 μm. During the first reflow process, the solder balls were immersed in a commercial NC-559-ASM type flux and then soldered onto the Cu pad on the package attachment side. This process involved a peak temperature of 240 °C and a holding temperature above the liquidus point (196 °C) for 80 s (see Fig. 1(e) for reference). For the second reflow process, the dummy chip was placed on the Cu pad of the PCB with a peak temperature of 240 °C and a holding temperature above the liquidus (196 °C) for 90 s (see Fig. 1(f)). The SnPb eutectic solder balls, with a diameter of 400 μm, were surface-mounted onto the Cu pad utilizing the thermal reflow profile indicated in Fig. 1(e). The size of the ball grid array (BGA) construction shear specimens was 17 mm × 17 mm (see Fig. 1(d)).

2.2 Irradiation test

The irradiation experiments adopted a DD1.2 high-frequency, high-voltage electron accelerator and yzn-02 ^{60}Co source irradiation equipment. The FIB and shear specimens were exposed to 200 h of γ-ray irradiation from a ^{60}Co source, 200 h of γ-ray irradiation and electron irradiation with a fluence of 2×10^{15} electrons/cm^2, and 200 h of γ-ray irradiation and electron irradiation with a fluence of 4×10^{15} electrons/cm^2. All irradiation experiments were performed under room temperature conditions. The γ-ray irradiation dose rate was set to be 1 Gy(Si)/s, pre-determined through dosimetry measurements, and the electron irradiation flux was

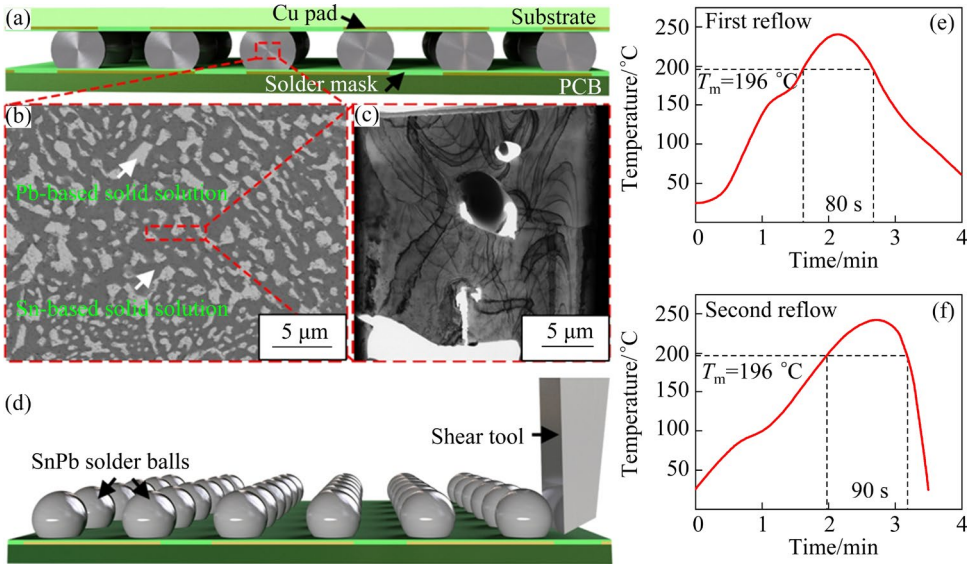

Fig. 1 Schematics of FIB and shear specimens: (a) Cross-section of SnPb eutectic solder joint; (b) Surface of unirradiated solder joint; (c) Unirradiated FIB specimen; (d) Shear specimen; (e) Reflow profile for first reflow; (f) Reflow profile for second reflow

set to be 1×10^{12} electrons/(cm^2·s). The average energy of the γ-ray was 1.25 MeV and the electron beam energy was 1.2 MeV.

2.3 Solder ball shear test and TEM observation

The solder ball shear tests were conducted using the DAGE 4000 ball shear system (Dage Precision Industries Co., Ltd., Aylesbury, UK). The nominal ball shear test speed was set as 120 μm/s with a shear height of 40 μm. Ten solder balls from each shear specimen were selected for shear testing under each irradiation condition. Load−displacement graphs were plotted for each sheared ball, and the average shear force and shear strength were subsequently calculated. A Talos F200X TEM instrument operating at 200 kV was adopted to characterize the detailed microstructures of the FIB specimen. For the purpose of eliminating variables introduced by distinct specimens, the same FIB specimen was observed under various irradiation time and in-situ TEM analysis was performed on the areas of interest (IAs). The thickness and area of the amorphous layer observed in high-resolution transmission electron microscopy (HRTEM) images were measured using ImageJ software.

3 Results

3.1 Mechanical properties of solder balls

Figure 2 and Table 1 illustrate the average shear strength and data of SnPb solder balls under various irradiation conditions. The average shear strength of the unirradiated specimen is 46.74 MPa. Following 200 h of γ-ray irradiation, the average shear strength increases by 10.10% to 51.46 MPa. Nonetheless, upon 200 h of γ-ray irradiation combined with electron irradiation at a fluence of 2×10^{15} electrons/cm^2, the average shear strength decreases by 3.53%, resulting in a value of 49.64 MPa. Additionally, after 200 h of γ-ray irradiation and electron irradiation at a fluence of 4×10^{15} electrons/cm^2, the average shear strength further decreases by 4.77%, bringing it to 47.27 MPa.

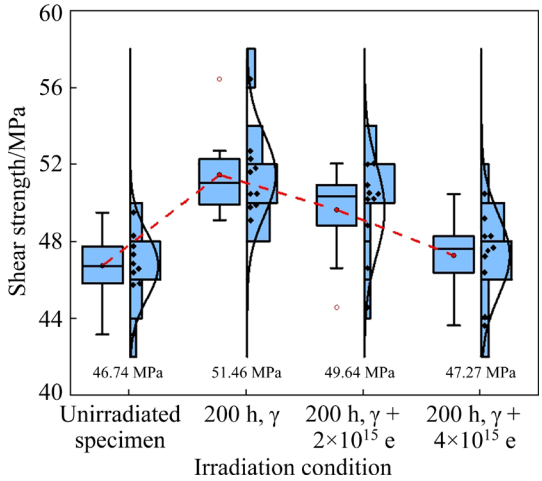

Fig. 2 Box plot of shear strength of SnPb eutectic solder balls under various irradiation conditions

Figure 3 illustrates the load−displacement graphs and SEM images at low and high magnifications, depicting the fracture morphology of shear specimens under distinct irradiation conditions. As demonstrated in Figs. 3(a−d), the shear force values gradually decrease following their peak rather than dropping abruptly to zero in all load−displacement graphs, which implies that under various irradiation conditions, the SnPb eutectic shear specimens undergo ductile fracture rather than brittle fracture. The fracture morphology in Figs. 3(e−h) exhibits typical features of ductile fracture, implying that the solder balls experienced ductile fracture. Prior studies have suggested that a steeper slope before and after the peak shear force in a load−displacement curve is indicative of a more brittle fracture mode [15,16], as it reflects a rapid loss of load-bearing capacity, characteristic of brittle materials. Besides, from the load−displacement graphs in Figs. 3(a) and (b), it is evident that after 200 h of γ-ray irradiation, the slope of the shear force decrease becomes steeper after reaching the peak value. Following electron irradiation with fluences of 2×10^{15} and 4×10^{15} electrons/cm^2, the slope of the shear force value decrease becomes flatter after reaching the maximum (refer to Figs. 3(b−d)), which implies that γ-ray irradiation reduces the plasticity of the solder balls, while subsequent electron irradiation enhances their plasticity. As demonstrated in Fig. 3(i), the unirradiated solder ball displays numerous large dimples on the fracture surface. Nevertheless, after 200 h of γ-ray irradiation, both the number and size of dimples on the shear fracture surface are diminished, as shown in Fig. 3(j). Upon

Table 1 Shear strength of SnPb eutectic solder balls under various irradiation conditions (Unit: MPa)

Irradiation condition	Ball #1	Ball #2	Ball #3	Ball #4	Ball #5	Ball #6	Ball #7	Ball #8	Ball #9	Ball #10
Unirradiated specimen	48.30	43.16	49.50	47.74	46.38	46.84	47.32	45.74	46.57	45.80
200 h, γ irradiation	51.61	56.44	50.47	49.90	52.29	49.77	52.71	50.47	51.81	49.10
200 h, γ + 2×10^{15} e irradiation	46.61	50.21	48.83	50.52	52.00	50.93	52.05	44.57	50.19	50.46
200 h, γ + 4×10^{15} e irradiation	48.27	50.46	44.06	47.52	43.62	47.68	48.27	47.22	46.38	49.19

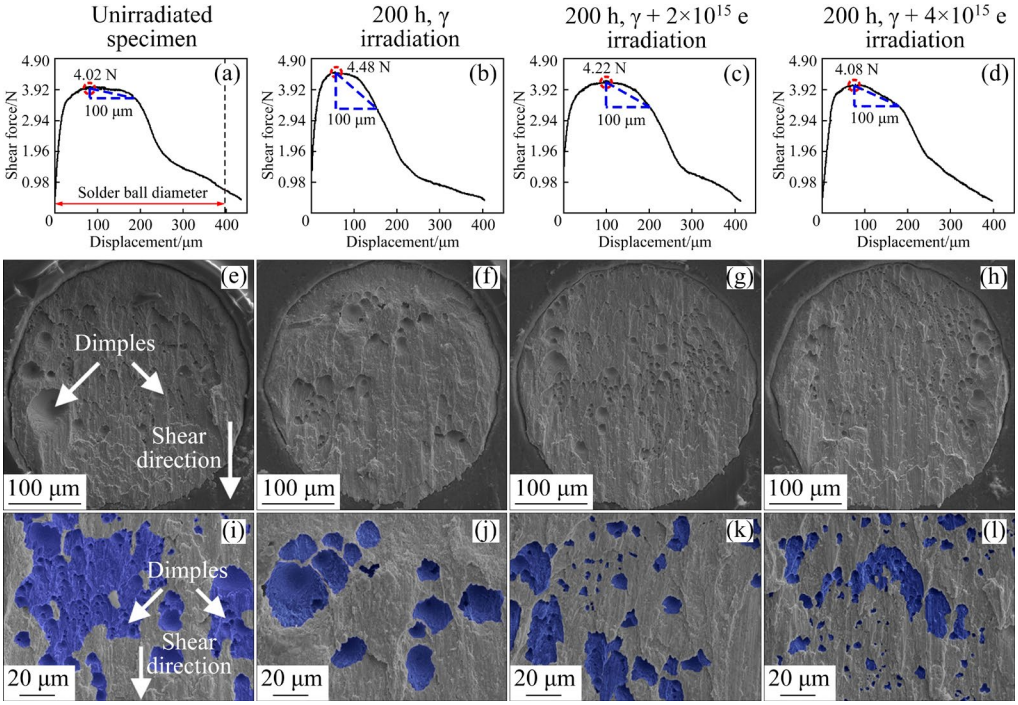

Fig. 3 Load−displacement graphs and fracture morphology images of sheared solder balls under various irradiation conditions: (a−d) Load−displacement graphs; (e−h) Low-magnification SEM images of fracture morphology; (i−l) High-magnification SEM images of fracture morphology

electron irradiation with fluences of 2×10^{15} and 4×10^{15} electrons/cm^2, the number of dimples on the fracture surfaces increases (see Figs. 3(k) and (l)). The change in the number and size of dimples on the fracture surface of the solder joint further confirms that the γ-ray irradiation deteriorates the ductility of the solder joint, while the electron irradiation partially restores its ductility.

3.2 Microstructural evolution of SnPb eutectic solder joint

Figure 4 illustrates the bright field images (BFIs) of the area of interest (IA) in the unirradiated SnPb eutectic FIB specimen. Besides, the IA is highlighted by the red dotted square in Fig. 4(a), and the corresponding BFIs of the IA under various irradiation conditions are displayed in Figs. 4(b−e). Additionally, the selected area electron diffraction (SAED) patterns of the BFIs in Figs. 4(b−e) are presented in Figs. 4(f−i), respectively. As revealed in Fig. 4(f), the SAED pattern of the unirradiated FIB specimen reveals merely a set of diffraction spots corresponding to the [012] zone axis of the β-Sn phase, which are highlighted by solid orange circles. After 200 h of γ-ray irradiation, polycrystalline diffraction rings corresponding to SnO_2 (highlighted with red dotted arcs) are observed in the SAED pattern alongside the diffraction spots of the β-Sn crystal with the [012] zone axis (refer to Fig. 4(g)). After electron irradiation at fluences of 2×10^{15} and 4×10^{15} electrons/cm^2, the polycrystalline diffraction rings of SnO_2 disappear from the SAED patterns (refer to Figs. 4(h) and (i)). Only the diffraction spots corresponding to the [012] zone axis of β-Sn are observed, with no additional diffraction spots or amorphous rings present, which indicates that the SnO_2 polycrystals have been reduced to the β-Sn phase as a result of electron irradiation.

Figure 5 indicates the HRTEM images (refer to Figs. 5(a−d)) of the β-Sn crystal in the FIB specimen, along with the corresponding strain maps (refer to Figs. 5(e−h)). The strain maps, generated through geometric phase analysis (GPA), offer a two-dimensional visualization of the strain ε_{xy} (a relative value). The color scale indicates strain variations, where positive values represent tensile strain and negative values correspond to compressive strain. Regions of stress concentration are denoted by black dashed lines. As demonstrated in Fig. 5(a), the β-Sn single crystal lattice structure in the unirradiated FIB specimen exhibits no lattice defects, and the area and intensity of the stress concentration region are both minimal (refer to Fig. 5(e)). Following 200 h of γ-ray irradiation, numerous Moiré fringes (refer to

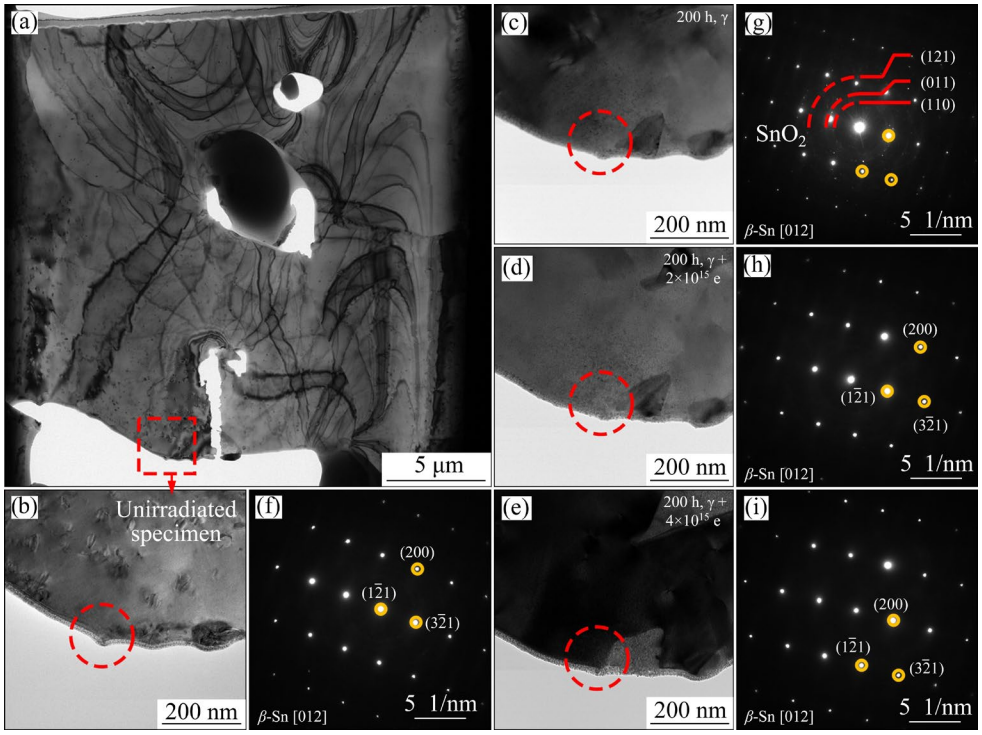

Fig. 4 BFIs and SAED patterns of FIB specimen under distinct irradiation conditions: (a) BFI of unirradiated FIB specimen; (b−e) BFIs of IA; (f−i) SAED patterns corresponding to red dotted circle regions in (b−e), respectively

Fig. 5(b)) and regions of stress concentration (refer to Fig. 5(f)) emerge in the β-Sn crystal. After electron irradiation at fluences of 2×10^{15} and 4×10^{15} electrons/cm^2, the Moiré fringes in the β-Sn crystal decrease and eventually disappear (refer to Figs. 5(c) and (d)) and the area of the stress concentration regions in the strain maps gradually decreases (refer to Figs. 5(g) and (h)).

Figure 6 indicates HRTEM images of IA in the FIB specimen under various irradiation conditions.

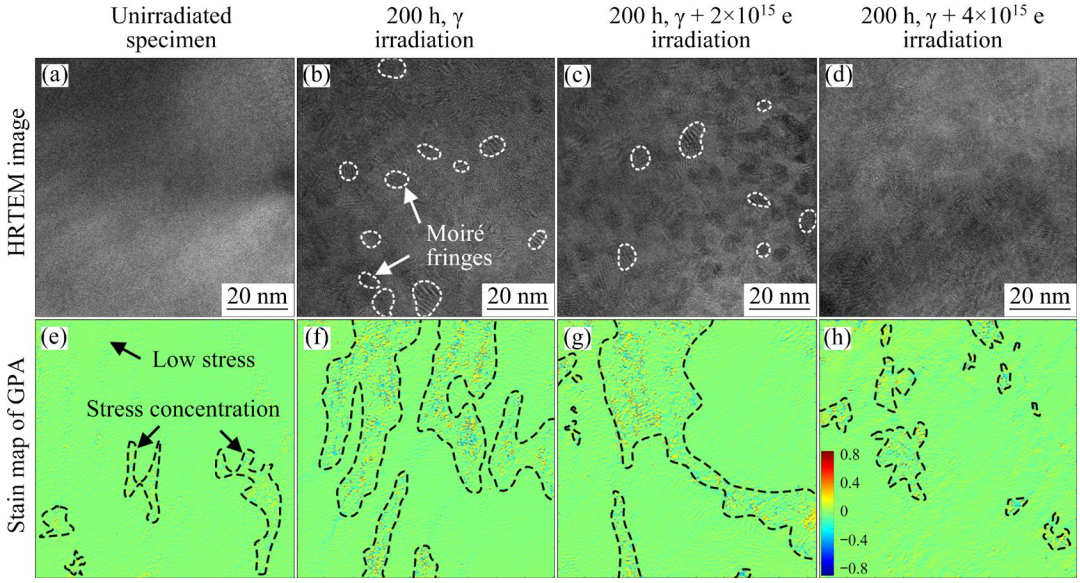

Fig. 5 HRTEM images (a−d) and corresponding strain maps (e−h) generated using GPA in FIB specimen under various irradiation conditions

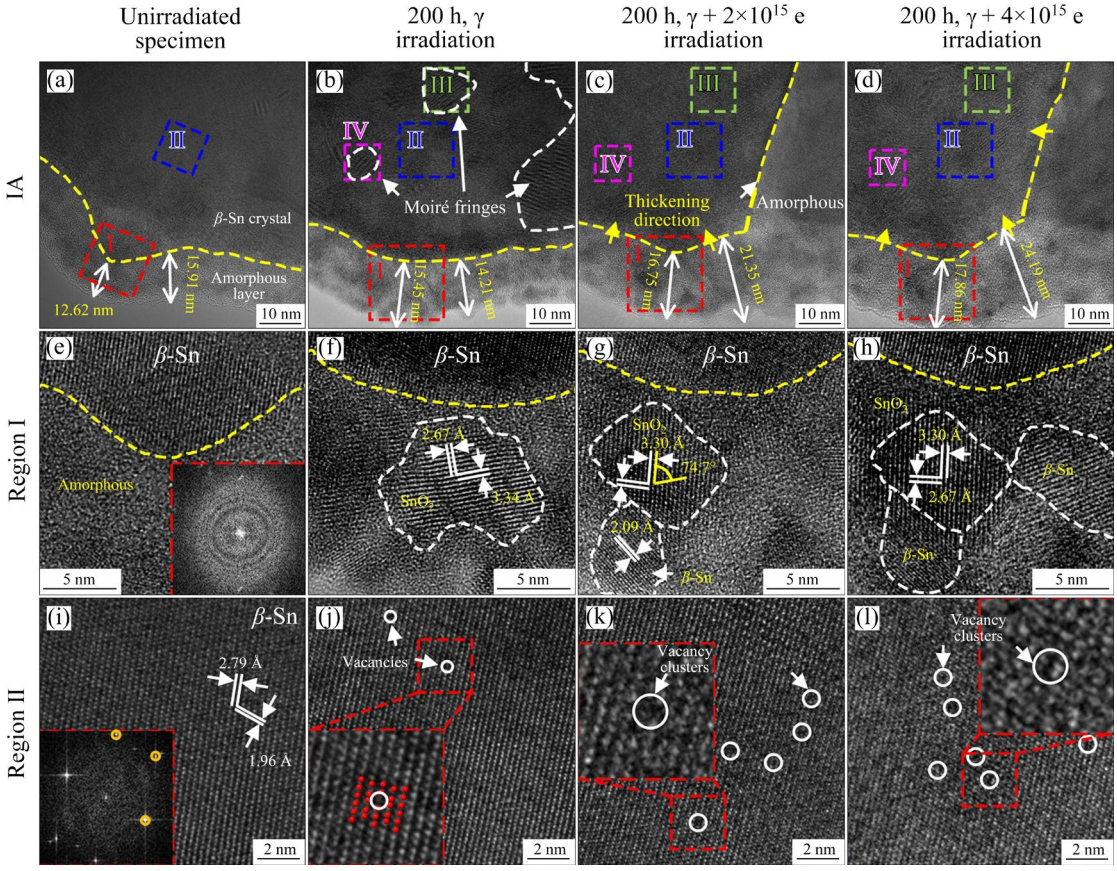

Fig. 6 HRTEM images of FIB specimen under distinct irradiation conditions: (a−d) HRTEM images of IA; (e−h) Magnified HRTEM images of Region I indicated by red dotted squares in (a−d), respectively; (i−l) Magnified HRTEM images of Region II indicated by blue dotted squares in (a−d), respectively

As demonstrated in Fig. 6(a), in the unirradiated FIB specimen, both the β-Sn crystal and an edge amorphous layer are visible. The initial amorphous layer is created by ion beam bombardment during the FIB process. The interfaces between the β-Sn crystal and the amorphous layer are highlighted by yellow dashed lines. The Fast Fourier Transform (FFT) diffraction pattern of the amorphous layer is shown in Fig. 6(e). After 200 h of γ-ray irradiation, Moiré fringes appear within the β-Sn crystal and the thickness of the amorphous layer increases. Following electron irradiation with fluences of 2×10^{15} and 4×10^{15} electrons/cm^2, the number and size of the Moiré fringes decrease and eventually vanish (refer to Figs. 6(c) and (d)). Additionally, the edge amorphous layer thickens towards the β-Sn crystal side, with the thickness increasing from 14.21 to 21.35 nm and then to 24.19 nm (refer to Figs. 6(a−d)). As demonstrated in Figs. 6(e) and (f), after 200 h of γ-ray irradiation, part of the amorphous structure crystallizes into SnO_2 nanocrystals. As the electron irradiation fluence increases, the size of the SnO_2 nanocrystals within the amorphous layer decreases, and β-Sn nanocrystals begin to form around the SnO_2 nanocrystal (refer to Figs. 6(g) and (h)). As indicated in Figs. 6(i) and (j), after 200 h of γ-ray irradiation, a small number of vacancies appear in the β-Sn single crystal. Following electron irradiation with a fluence of 2×10^{15} electrons/cm^2, the number of vacancies increases, and the vacancies aggregate to form clusters (refer to Fig. 6(k)). As the electron irradiation fluence increases to 4×10^{15} electrons/cm^2, both the number and size of the vacancy clusters also increase (refer to Fig. 6(l)).

Figure 7 indicates the HRTEM images, FFT patterns, inverse Fast Fourier Transform (IFFT) patterns, and strain maps of the IA, illustrating β-Sn crystal and edge amorphous layer under various irradiation conditions. As demonstrated in Figs. 7(a) and (a1), the β-Sn crystal with a [012] zone axis (refer to Fig. 7(e1)) is observed, and the selected amorphous region (highlighted with dashed yellow line) has an area of 273.45 nm^2. No vacancy or dislocation defects are observed in the β-Sn crystal, as indicated in the HRTEM images and IFFT patterns (refer to Figs. 7(a) and (e)). Additionally, there are no

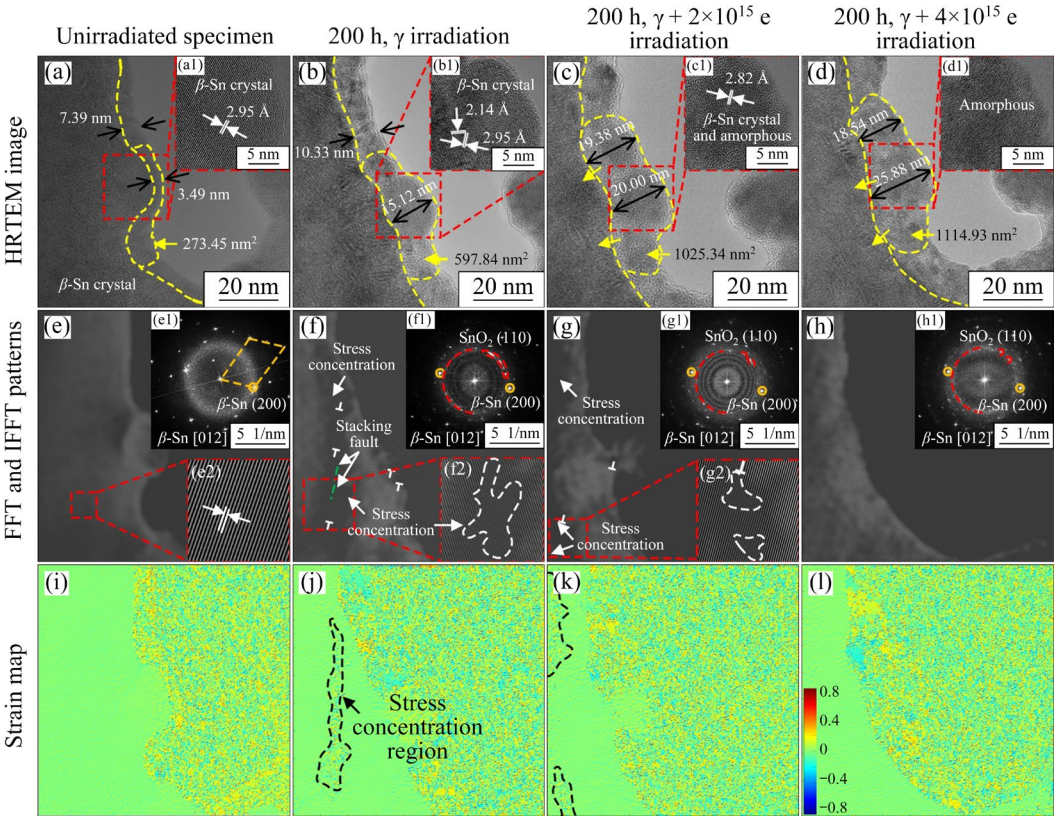

Fig. 7 HRTEM images, FFT patterns, IFFT patterns and strain maps of IA in FIB specimen under various irradiation conditions: (a−d) HRTEM images; (a1−d1) Magnified HRTEM images of red dotted square regions in (a−d), respectively; (e−h) IFFT images of $(200)_{\beta\text{-Sn}}$ plane of HRTEM images in (a−d), respectively; (e1−h1) FFT patterns of HRTEM images in (a−d), respectively; (i−l) Strain maps generated using GPA for HRTEM images in (a−d), respectively

stress concentration regions in the strain map (refer to Fig. 7(i)). Following 200 h of γ-ray irradiation, the thickness of the amorphous layer increases, and the area of the amorphous region expands to 597.84 nm^2 (refer to Fig. 7(b)). Polycrystalline diffraction rings corresponding to SnO_2 appear in the FFT pattern (refer to Fig. 7(f1)), indicating the presence of SnO_2 nanocrystals in the *β*-Sn crystal. Crystal defects including dislocation and stacking faults (refer to Fig. 7(f)), along with stress concentration regions (refer to Fig. 7(j)), likewise appear in the *β*-Sn crystal. After electron irradiation at fluences of 2×10^{15} and 4×10^{15} electrons/cm^2, the thickness of the amorphous layer continues to increase, and the area of the amorphous regions (refer to Figs. 7(c) and (d)) expands further to 1025.34 and 1114.93 nm^2, respectively. The region initially exhibiting a *β*-Sn single crystal lattice structure (refer to Fig. 7(b1)) transforms to an amorphous state (refer to Figs. 7(c1) and (d1)). As the electron irradiation fluence increases, the intensity of the SnO_2 polycrystalline diffraction rings decreases (refer to Figs. 7(g1) and (h1)), implying a partial reduction of the SnO_2 phase. Simultaneously, the number of dislocations and the area of stress concentration regions in the *β*-Sn crystal gradually decrease (refer to Figs. 7(g) and (k)). On the condition that the electron irradiation fluence reaches 4×10^{15} electrons/cm^2, dislocation and stress concentration regions disappear in the *β*-Sn crystal (refer to Figs. 7(h) and (l)). In summary, after γ-ray and electron irradiation, the thickness of the amorphous layer in the FIB specimen increases. Meanwhile, the number of dislocations, the SnO_2 phase, and stress concentration regions initially increase (after 200 h of γ-ray irradiation) and subsequently decrease (after electron irradiation at fluences of 2×10^{15} and 4×10^{15} electrons/cm^2).

Figure 8 demonstrates HRTEM images and the corresponding FFT and IFFT patterns of two typical Moiré fringes that appear in the *β*-Sn crystal following 200 h of γ-ray irradiation. Figures 8(a) and (f) provide an enlarged view of the two Moiré fringes in Regions III and IV in Figs. 6(b−d), respectively. Moiré fringe patterns are formed in TEM images on the condition that one crystal overlays another, indicating a mismatch in the lattice spacing between the two crystals, which serves as an effective method for sensitive local strain measurement [17−20]. The mechanism behind the generation of Moiré fringes in the *β*-Sn crystal following 200 h of γ-ray irradiation

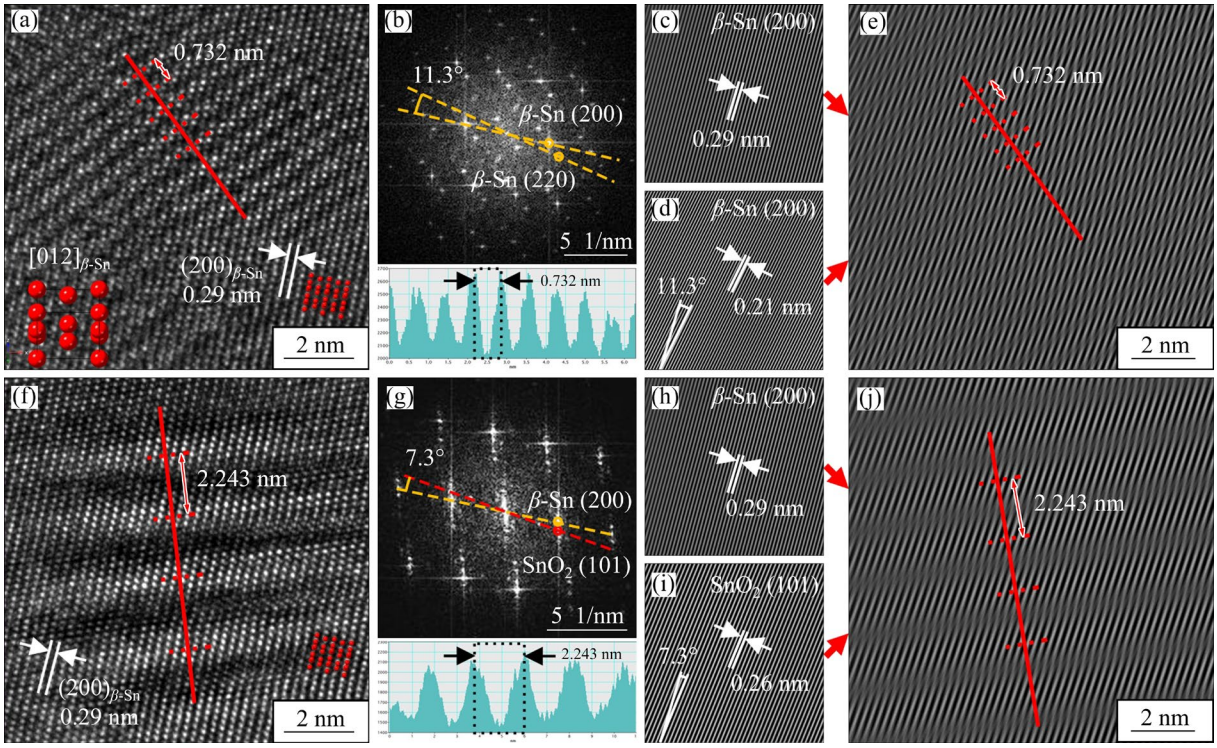

Fig. 8 Two typical Moiré fringes in *β*-Sn crystal following 200 h of γ-ray irradiation: (a, f) HRTEM images of Moiré fringes; (b, g) FFT patterns corresponding to (a, f), respectively; (c, h) IFFT patterns of (200) plane of *β*-Sn corresponding to (a, f), respectively; (d, i) IFFT patterns of (220) plane of *β*-Sn and (101) plane of SnO_2 corresponding to (a, f), respectively; (e, j) Moiré fringe simulation images from IFFT patterns in (c, d, h, i), respectively

has been elucidated in our previous research [13]. This work explores the orientation relationship between surface and internal crystal planes. The distorted or disordered lattice fringes can be calculated using the following equation [21]:

$$d_m=\frac{d_1d_2}{\sqrt{(d_1-d_2)^2+d_1d_2\beta^2}} \quad (1)$$

where d_m represents Moiré fringe periodic spacing, d_1 and d_2 are the lattice spacings of the planes that are the constituents of the Moiré fringes, and β is the angle between the planes. Besides, the values of d_m, d_1 and β in Figs. 8(a, b, f, g) are 0.732 nm, 0.29 nm and 11.3°, and 2.243 nm, 0.29 nm and 7.3°, respectively. When the above values are substituted into Eq. (1), the calculation results indicate that the Moiré fringes in Fig. 8(a) result from the overlapping of the $(200)_{\beta\text{-Sn}}$ and $(220)_{\beta\text{-Sn}}$ planes, while the Moiré fringes in Fig. 8(f) result from the overlapping of the $(200)_{\beta\text{-Sn}}$ and $(101)_{SnO_2}$ planes. The IFFT patterns of the $(200)_{\beta\text{-Sn}}$ (refer to Fig. 8(c)) and $(220)_{\beta\text{-Sn}}$ (refer to Fig. 8(d)) planes, as well as the IFFT patterns of the $(200)_{\beta\text{-Sn}}$ (refer to Fig. 8(h)) and $(101)_{SnO_2}$ (refer to Fig. 8(i)) planes, are overlapped, with the angles between the planes set to be 11.3° and 7.3°. The resulting Moiré fringe patterns in Figs. 8(e) and (j) are consistent with the Moiré fringes observed in the HRTEM images (refer to Figs. 8(a) and (f)).

4 Discussion

4.1 Interaction between electron irradiation and SnPb eutectic solder joints

4.1.1 Simulation of 1.2 MeV electron penetration depth in β-Sn and Pb metals

The electronegativity difference between Sn and Pb is minimal, which inhibits the formation of intermetallic compounds. Instead, Sn and Pb dissolve into each other, forming solid solutions. The concentrations of Sn and Pb in Pb-based and Sn-based solid solutions are quite low, allowing the electron irradiation process on SnPb eutectic solder joints to be approximated as irradiation on pure β-Sn and Pb metals. The paths (refer to Figs. 9(a) and (c)) and energy loss maps (refer to Figs. 9(b) and (d)) of the incident electrons were simulated using CASINO software, which employs the Monte Carlo method. The simulation was conducted with 2000 incident electrons, a beam diameter of 10 nm, and an energy of 1.2 MeV, applied to pure β-Sn and Pb metals. As indicated in Figs. 9(b) and (d), the electron energy is not uniformly distributed with increasing the penetration depth. Taking 50% of the electron energy loss as the equivalent incident depth, the penetration depth of 1.2 MeV electrons in β-Sn and Pb is about 173.88 and 96.04 μm, respectively, which suggests

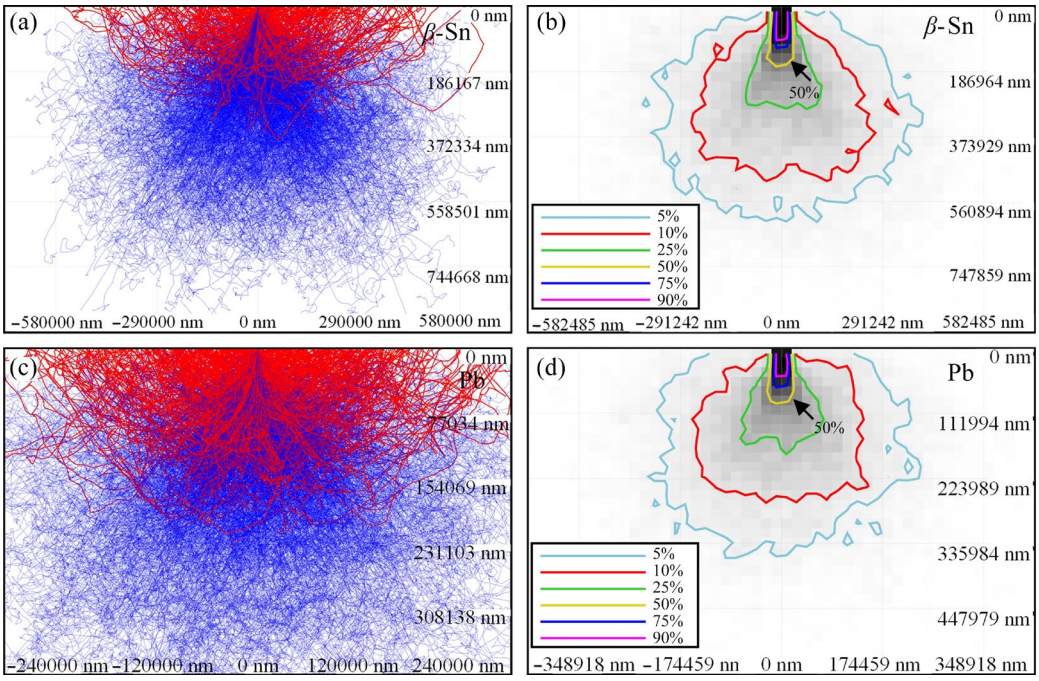

Fig. 9 Incident electron path (a, c) and energy loss distribution (b, d) maps for 1.2 MeV electrons in β-Sn and Pb

that, although electrons exhibit limited penetration ability in metals, they still penetrate SnPb eutectic solder joints with a radius of 200 μm and interact with Sn and Pb atoms, thereby influencing the microstructure evolution and mechanical properties of the solder joints.

4.1.2 Interaction mechanism between electrons and Sn and Pb atoms

The maximum energy transferred by electrons to the target atom (E_m) can be determined by [22]

$$E_m=\frac{2E_e(E_e+2m_ec^2)}{Mc^2} \tag{2}$$

where M demonstrates the mass of the target atom, E_e indicates the electron energy (1.2 MeV), c reveals the speed of light, m_e is the rest mass of electron, and m_ec^2 illustrates the electron rest energy with the value of 0.511 MeV. Substituting the given parameters into Eq. (2), the calculated values of E_m for Sn and Pb atoms are 48.48 and 27.66 eV, respectively. Besides, the average displacement threshold energy (E_d) of Sn and Pb atoms is (22±2) eV [23] and (25±5) eV [24], respectively, which suggests that electrons with an energy of 1.2 MeV are capable of displacing the Sn and Pb atoms in the FIB specimen.

The cross-section area between an electron and a target atom (σ_s) can be calculated by [22]

$$\sigma_s=\frac{4\pi a_0^2Z^2E_R^2}{m_e^2c^4}\left(\frac{1-\beta_1^2}{\beta_1^2}\right)\left(\frac{E_m}{E_d}-1\right) \tag{3}$$

where a_0 reveals the Bohr radius of the atom (0.053 nm), Z signifies the atomic number, E_R indicates Rydberg energy (13.606 eV), and β_1 demonstrates the ratio of the velocity of an incident electron to the speed of light, with a value of 0.90. Substituting the given parameters into Eq. (3), the cross-section areas for interactions between electrons and β-Sn and Pb atoms are 4.9×10^{-23} and 3.55×10^{-23} cm^2, respectively.

The number of atoms displaced per unit volume by electrons (N_s) can be determined utilizing Eq. (4) [22]:

$$N_s=f\sigma_sN_0I_et \tag{4}$$

where f demonstrates the number of displacements induced by an incident electron, N_0 reveals the number of atoms per unit volume, I_e is the electron flux, t is the irradiation time, and I_et represents the fluence of electron irradiation. Frenkel vacancy pairs are the primary defects induced in metal crystals by electron irradiation [25], which is why the value of f is set to 1. Substituting the given parameters into Eq. (4), the numbers of displaced Sn atoms in 1 cm^3 of β-Sn exposed to electron irradiation fluences of 2×10^{15} and 4×10^{15} electrons/cm^2 are 3.62×10^{15} and 7.24×10^{15} atoms/cm^3, respectively. Comparably, the numbers of displaced Pb atoms in 1 cm^3 of Pb exposed to the identical electron irradiation fluences are 2.34×10^{15} and 4.68×10^{15} atoms/cm^3, respectively.

4.2 Formation mechanism of γ-ray and electron irradiation induced amorphous phase in SnPb eutectic solder joints

As discussed above, the amorphous phase in the FIB specimen increases following γ-ray and electron irradiation. The increase in the amorphous phase induced by these irradiations manifests in two key aspects: the transformation from β-Sn crystal to amorphous phase (C−A), and the growth in the thickness of the amorphous layer. Concerning the first aspect, it is widely recognized that energetic particle bombardment of solid surfaces can lead to the accumulated structural damage, promoting amorphization. In our study, after the FIB specimen was subjected to 200 h of γ-ray and electron irradiation with fluences of 2×10^{15} and 4×10^{15} electrons/cm^2, the lattice defects induced by both irradiations accumulated in the β-Sn crystal. When the defect concentration reaches a critical value, the lattice structure becomes unstable and leads to amorphization. From a thermodynamic perspective, the C−A transformation of β-Sn occurs when the increase in the free energy of the original β-Sn crystal phase, resulting from the energy injection from γ-ray and electron irradiation, reaches a value that is equal to or greater than the free energy of the amorphous phase [26].

The following analyzes the second aspect. Figure 10 provides a schematic diagram illustrating the mechanism behind the increase in amorphous layer thickness during γ-ray and electron irradiation. Moreover, the β-Sn crystal/amorphous (C/A) interface is highlighted with solid blue lines. It is well recognized that dislocations, phase interfaces, and grain boundaries (GBs) serve as defect sinks, absorbing nearby point defects such as vacancies and interstitials. As defect sinks, the C/A interfaces continuously absorb point defects generated by γ-ray and electron irradiation in both the β-Sn crystal and the amorphous phase (refer to Fig. 10(a)). Since the

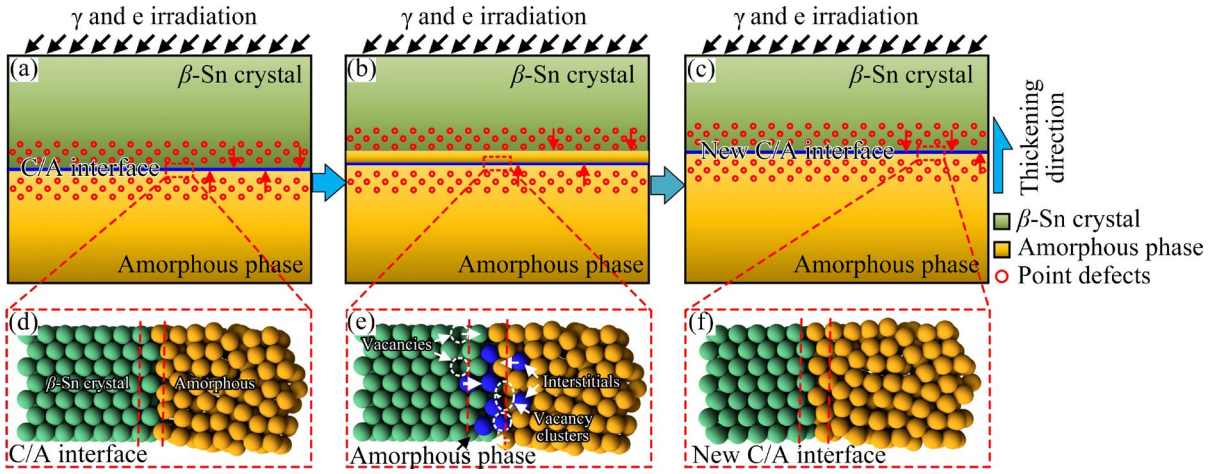

Fig. 10 Schematic diagrams of increase in amorphous layer thickness: (a) Point defects generated by γ-ray and electron irradiation; (b) Movement of point defects to C/A interface and amorphization of *β*-Sn crystal near C/A interface; (c) Formation of new C/A interface; (d−f) Schematic representation of C/A interface evolution corresponding to (a−c)

lattice structure around the C/A interface is incomplete and unstable, atomic displacements are more likely to occur during high-energy particle collisions. Amorphization occurs in the *β*-Sn crystal near the C/A interface (refer to Figs. 10(b) and (e)), eventually forming a new C/A interface (refer to Figs. 10(c) and (f)), resulting in increased amorphous layer thickness. Hence, during electron irradiation, a continuous process occurs: point defects generated by electron irradiation → migration of defects to the C/A interface → amorphization of the *β*-Sn crystal near C/A interface → formation of a new C/A interface, which leads to a progressive increase in the thickness of the amorphous layer.

4.3 Mechanism of rotation of *β*-Sn and reduction of SnO_2 nanocrystals induced by electron irradiation

As shown in Fig. 8, following 200 h of γ-ray irradiation, the Moiré fringes in Regions III and IV (refer to Figs. 6(b−d)) are caused by the overlap of the (220) plane of internal *β*-Sn nanograin and the (101) plane of the internal SnO_2 nanocrystal with the (200) plane of surface *β*-Sn crystal. After electron irradiation, the Moiré fringes in Regions III and IV disappear, as observed in Figs. 6(b−d). Additionally, the analysis of Figs. 5−7 demonstrates that the number and size of the Moiré fringes in the FIB specimen gradually decrease and eventually disappear following electron irradiation with fluences of 2×10^{15} and 4×10^{15} electrons/cm^2. Since the surface of the *β*-Sn crystal always maintains the (200) plane before and after irradiation (refer to Fig. 6), it can be concluded that the internal *β*-Sn and SnO_2 nanograins undergo lattice rotation and reduction after electron irradiation, respectively. The mechanism of internal *β*-Sn nanocrystal rotation is as follows: the rotation and coalescence of nanocrystals act as a process for defect reduction, involving vacancies, dislocations, and GBs [27,28]. During electron irradiation, the GBs between the internal *β*-Sn nanograin with the (200) plane and the surface *β*-Sn crystal with the (220) plane act as defect sinks, continuously absorbing point defects generated by the irradiation. As the electron irradiation fluence increases, point defects accumulate at the GBs and eventually cause them to collapse. This results in the rearrangement of Sn atoms within the GBs, along with the migration and reduction of dislocations (refer to Figs. 11(b) and (c)), and the gradual disappearance of the GBs (refer to Fig. 11(d)) [29].

Combining the analysis of Figs. 4 and 8, it can be concluded that electron irradiation results in the

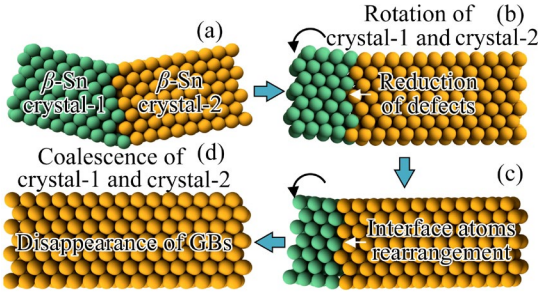

Fig. 11 Schematic diagrams of *β*-Sn nanograins undergoing rotation and coalescence during electron irradiation

reduction of SnO_2 on the surface and within the FIB specimen. The reduction mechanism of SnO_2 nanocrystals in the β-Sn crystal is as follows.

Microscopically, the reduction of metal oxides involves the removal of lattice oxygen, followed by the structural rearrangement of the parent lattice. The reduction activity is assessed by the energy required to remove lattice oxygen, which is referred to as the vacancy formation energy [30]. The O vacancy formation energy in SnO_2 ranges between 2 and 3 eV, which is substantially smaller than the E_d of Sn, which is 22 eV. This implies that compared to Sn atoms, incident electrons with an energy of 1.2 MeV are more likely to displace O atoms, resulting in the creation of O vacancies. Under γ-ray and electron irradiation, γ photons and electrons collide with Sn and O atoms, generating a small number of Sn lattice vacancies and a large number of O lattice vacancies in SnO_2. This effect is especially noticeable at the interface between β-Sn and SnO_2, where a high concentration of crystal defects and broken bonds result in lower vacancy formation energy, facilitating easier atomic displacement. In our case, point defects, including Sn and O vacancies as well as interstitial atoms, migrate towards the β-Sn/SnO_2 interface (refer to Fig. 12(b)). During this process, Sn and O vacancies accumulate and cluster at the interface, eventually collapse. Interstitial O atoms combine into O_2 molecules and exit the crystal surface, resulting in a reduction in SnO_2 size and rotation (refer to Fig. 12(b)). Sn interstitial atoms migrate to the β-Sn/SnO_2 interface, where they aggregate, rearrange and nucleate, eventually forming β-Sn nanograins around the SnO_2 (refer to Fig. 12(c)). The reduction process of SnO_2 nanocrystal in β-Sn amorphous phase (refer to Figs. 6(f−h)), which is comparable to the reduction process of SnO_2 nanocrystal in the β-Sn crystal, is demonstrated in Figs. 12(d−f).

4.4 Mechanical property evolution mechanism of solder balls after γ-ray and electron irradiation

4.4.1 Mechanism of internal stress evolution in β-Sn crystal

As illustrated in strain maps in Figs. 5 and 7, after γ-ray and electron irradiation, the internal stress in the β-Sn crystal within the FIB specimen first increases and subsequently decreases. Previous research has indicated that γ-ray irradiation leads to the oxidation of the β-Sn crystal. SnO_2 has a larger specific phase volume than β-Sn, and when β-Sn is fully oxidized to SnO_2, its volume expands by approximately 31% [13]. The initial increase in internal stress is due to the volume expansion during the transformation of β-Sn into SnO_2. Under electron irradiation, some SnO_2 is partially reduced to β-Sn, resulting in the disappearance of the internal stress caused by the volume expansion. Similar to the mechanism of metal annealing, the reduction in internal stress leads to the slip and reorganization of dislocations. This aligns with the observed decrease in dislocation density in the β-Sn crystal following electron irradiation, as shown in the IFFT images (refer to Figs. 7(e−h)).

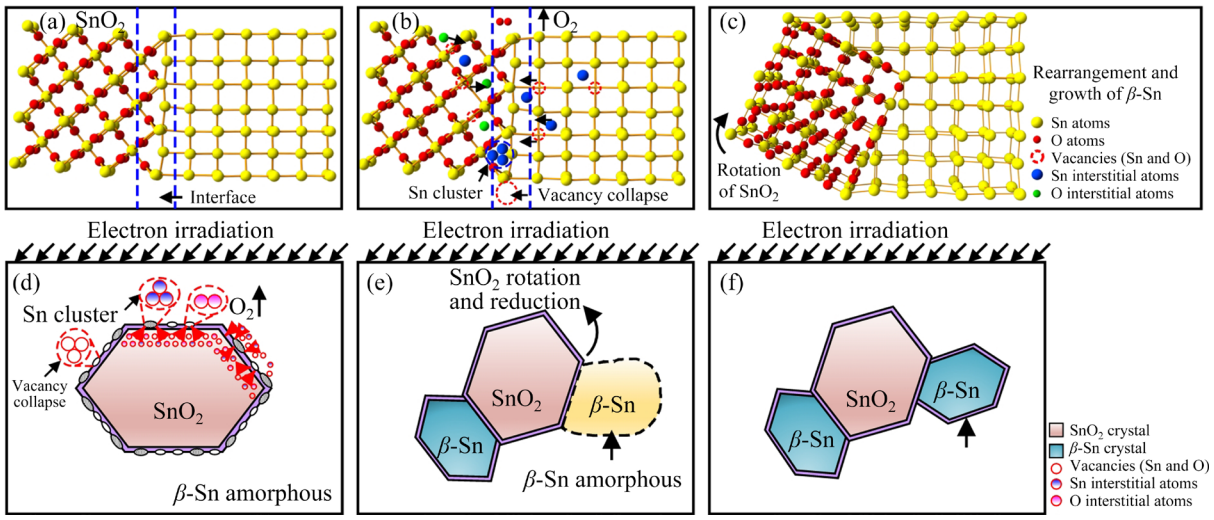

Fig. 12 Schematic diagrams of SnO_2 reduction process: (a−c) Reduction process of SnO_2 in β-Sn crystal; (d−f) Reduction process of SnO_2 in amorphous phase

4.4.2 Mechanism of mechanical property evolution of solder balls after γ-ray and electron irradiation

As demonstrated in Fig. 2 and 3, after γ-ray and electron irradiation, the shear strength of the solder balls first increases and then decreases, while plasticity initially decreases and later increases. The initial increase in shear strength and decrease in the plasticity of the solder balls can be attributed to the formation of SnO_2 within the β-Sn crystal, which contributes to the dispersion strengthening of the solder ball, as previously analyzed [14]. Following electron irradiation, the shear strength of the solder balls decreases, while plasticity increases. This change in mechanical properties is influenced by three key factors: Firstly, part of the β-Sn crystal transforms into an amorphous phase within the solder balls due to electron irradiation. Furthermore, LI and LI [31] proposed a "local volume increase → local shear softening → large local strain → local volume increase" loop in the amorphous deformation process. During shearing, the shear softening of the β-Sn amorphous region in the solder ball results in a decrease in shear strength. Secondly, some SnO_2 nanocrystals are reduced to β-Sn within the solder ball, resulting in a reduction in both the number and size of the SnO_2 nanocrystals. Previous studies have indicated that the SnO_2 nanocrystals in the β-Sn matrix, induced by γ-ray irradiation, contribute to the dispersion-strengthening effect of the solder ball [13]. The reduction of SnO_2 weakens the dispersion strengthening effect, resulting in decreased shear strength and increased plasticity of the solder ball. Finally, the reduction in dislocation density within the solder balls contributes to the decrease in shear strength and the enhancement of plasticity.

5 Conclusions

(1) SnPb eutectic FIB and shear specimens were subjected to 200 h of γ-ray irradiation and electron irradiation at fluences of 2×10^{15} and 4×10^{15} electrons/cm^2 to investigate their effects on microstructure and mechanical properties.

(2) Electron irradiation caused the disappearance of SnO_2 polycrystalline diffraction rings in the SAED pattern of the FIB specimen, indicating the reduction of SnO_2 nanocrystals to β-Sn.

(3) Electron irradiation increased point defects, including vacancies and vacancy clusters, while reducing line and surface defects, including dislocations, stacking faults, GBs, and phase interfaces, in β-Sn.

(4) Following electron irradiation, part of the β-Sn crystal transformed into an amorphous phase, and the amorphous layer thickened toward the β-Sn crystal. The electron-irradiated β-Sn crystal demonstrated a decrease in the number and area of stress concentration regions.

(5) After γ-ray and electron irradiation, the average shear strength of the solder balls initially increased by 10.10%, then decreased by 3.53% and 4.77%, respectively, and the plasticity and the number of dimples on the fracture surfaces of the solder balls initially reduced and then increased.

(6) The reduction in Moiré fringes within the β-Sn crystal was attributed to the rotation and coalescence of β-Sn nanocrystals and the reduction of SnO_2.

CRediT authorship contribution statement

Qi-long GUAN: Conceptualization, Methodology, Validation, Writing − Original draft, Investigation; **Chun-jin HANG:** Writing − Review & editing, Resources, Funding acquisition, Methodology, Supervision; **Wei ZHANG:** Validation, Formal analysis, Supervision; **Sheng-li LI:** Investigation; **Xiao-jiu TANG:** Investigation; **Dan YU:** Supervision, Funding acquisition, Data curation; **Ying DING:** Supervision, Funding acquisition, Formal analysis; **Xiu-li WANG:** Supervision, Funding acquisition, Validation; **Yu-bao ZHANG:** Funding acquisition, Resources, Supervision.

Declaration of competing interest

The authors declare that they have no known competing financial interests or personal relationships that could have appeared to influence the work reported in this paper.

Acknowledgments

This work was financially supported by the National Natural Science Foundation of China Young Student Basic Research Program (for Ph.D. students) (No. 525B2069), the Fundamental Research Funds for the Central Universities, China (No. HIT.DZJJ.2025005), and the National Key Laboratory of Precision Welding & Joining of Materials and Structures Research Project, China (No. 24-Z-09).

References

[1] LIU Jin-hong, XU Jian-hao, PAIK K, HE Peng, ZHANG Shu-ye. In-situ isothermal aging TEM analysis of a micro Cu/ENIG/Sn solder joint for flexible interconnects [J]. Journal of Materials Science & Technology, 2024, 169: 42−52.

[2] WU Jie, HUANG Huo-qiang, XUE Song-bai, XUE peng, XU Yong. Thermal reliabilities of Sn−0.5Ag−0.7Cu−0.1Al_2O_3/Cu solder joint [J]. Transactions of Nonferrous Metals Society of China, 2022, 32: 3312−3320.

[3] XU Da, SHEN Fei, ZHANG Yu, WANG Li-wei, YANG Xiao, LIANG Zhi-min. Effect of Ag and Cu co-addition on the microstructure evolution, interface behavior and mechanical properties of Sn−5Sb based solder joints subjected to different thermal aging conditions [J]. Microelectronics Reliability, 2022, 139: 114797.

[4] WU Ming, WANG Shan-lin, YIN Li-meng, CHEN Yu-hua, HONG Min, SUN Wen-jun, YAO Zong-xia, NI Jia-ming, LU Peng, ZHANG Ti-ming, XIE Ji-lin. Oxidation behavior and intermetallic compound growth dynamics of SAC305/Cu solder joints under rapid thermal shock [J]. Transactions of Nonferrous Metals Society of China, 2023, 33: 3054−3066.

[5] PENG Chen, WANG Shan-lin, WU Ming, YIN Li-meng, CHEN Yu-hua, YE Ke-jiang, CHEN Wei-zheng, ZHANG Ti-ming, XIE Ji-lin. Effect of Ag content on microstructure and mechanical properties of Sn−*x*Ag−0.5Cu solder joints under rapid thermal shock [J]. Transactions of Nonferrous Metals Society of China, 2024, 34: 1922−1935.

[6] LI Sheng-li, HANG Chun-jin, ZHANG Wei, GUAN Qi-long, TANG Xiao-jiu, YU Dan, DING Ying, WANG Xiu-li. Current-induced solder evolution and mechanical property of Sn−3.0Ag−0.5Cu solder joints under thermal shock condition [J]. Journal of Alloys and Compounds, 2024, 970: 172519.

[7] LI Sheng-li, HANG Chun-jin, GUAN Qi-long, TANG Xiao-jiu, YU Dan, DING Ying, WANG Xiu-li. The microstructure evolution and failure mechanism of Sn37Pb solder joints under the coupling effects of extreme temperature variation and electromigration [J]. Materials Today Communications, 2023, 36: 106651.

[8] LEHAN N, YUSOFF W, SOBRI N, AHMAD K, ABDULLAH M, AMAT A, JALAR A, RAHMAN I, SALLEH E. EDS analysis on effect of low dosage gamma radiation and micromechanical properties of $SnAg_3Cu_{0.5}$ solder [J]. Journal of Materials Science: Materials in Electronics, 2022, 33: 4225−4236.

[9] YUSOFF W, ISMAIL N, LEHAN N, AMAT A, AHMAD K, JALAR A, RAHMAN I. Micromechanical response of SAC305 solder alloy under gamma radiation via nanoindentation approach [J]. Soldering & Surface Mount Technology, 2023, 35(1): 51−58.

[10] WANG Jian-hao, XUE Song-bai, LV Zhao-ping, WANG Liu-jue, LIU Han, WEN Li. Effect of gamma-ray irradiation on microstructure and mechanical property of $Sn_{63}Pb_{37}$ solder joints [J]. Journal of Materials Science: Materials in Electronics, 2018, 29: 20726−20733.

[11] WANG Jian-hao, XUE Song-bai, LV Zhao-ping, WEN Li, LIU Si-yi. Study on the reliability of Sn50Pb49Sb1/Cu solder joints subjected to γ-ray irradiation [J]. Applied Sciences, 2018, 8(10): 1706.

[12] WANG Jian-hao, XUE Song-bai, LV Zhao-ping, WEN Li, LIU Si-yi. Microstructure and performance evolution of SnPbSb solder joint under γ-ray irradiation and thermal cycling [J]. Journal of Materials Science: Materials in Electronics, 2019, 30: 4990−4999.

[13] GUAN Qi-long, HANG Chun-jin, YAO Gang, LI Sheng-li, YU Dan, DING Ying, TIAN Yan-hong. Effect of gamma irradiation on microstructural evolution and mechanical properties of Sn3Ag0.5Cu solder joints [J]. Journal of Materials Research and Technology, 2023, 24: 6022−6033.

[14] GUAN Qi-long, HANG Chun-jin, LI Sheng-li, TANG Xiao-jiu, YAO Gang, YU Dan, DING Ying, WANG Xiu-li, ZHANG Wei. Effect of gamma irradiation on microstructural evolution and mechanical properties of SnPb eutectic solder joints [J]. Journal of Materials Research and Technology, 2023, 27: 2929−2938.

[15] SALLEH M, MCDONALD S, NOGITA K. Effects of Ni and TiO_2 additions in as-reflowed and annealed Sn0.7Cu solders on Cu substrates [J]. Journal of Materials Processing Technology, 2017, 242: 235−245.

[16] TSUKAMOTO H, NISHIMURA T, SUENAGA S, NOGITA K. Shear and tensile impact strength of lead-free solder ball grid arrays placed on Ni (P)/Au surface-finished substrates [J]. Materials Science and Engineering: B, 2010, 171(1/2/3): 162−171.

[17] WANG R Z, WEINER S. Strain−structure relations in human teeth using Moiré fringes [J]. Journal of Biomechanics, 1997, 31(2): 135−141.

[18] MURAKAMI Y, SASAKI TT, OHKUBO T, HONO K. Strain measurements from $Nd_2Fe_{14}B$ grains in sintered magnets using artificial moiré fringes [J]. Acta Materialia, 2015, 101: 101−106.

[19] WILLIAMS D B, CARTER C B. Transmission electron microscopy: A textbook for materials science [M]. 2nd ed. New York: Springer, 2009: 441−450.

[20] HIRSCH P, HOWIE A, NICHOLSON R, PASHLEY D, WHELAN M. Electron microscopy of thin crystals [M]. 2nd ed. Malabar, FL: Krieger, 1977: 353−378.

[21] FU Xiao-ling, DENG Ri-qiu, KONG Xiang-bin, PARANDE G, HU Ji-song, PENG Ping, ZHU Zhi-guang, SHI Bin-qing, WANG Gang, GUPTA M, RITCHIE R O. Interfacial characterization and its influence on the corrosion behavior of Mg−SiO_2 nanocomposites [J]. Acta Materialia, 2022, 230: 117840.

[22] MIURA K, FIORE N F, ALLEN C W. The influence of Mg in γ-irradiation induced changes in Al alloys [J]. Journal of Nuclear Materials, 1975; 55(1): 53−63.

[23] MCILWAIN J, GARDINER R, SOSIN A, MYHRA S. Low temperature electron-irradiation of β-tin [J]. Radiation Effects, 1975, 24: 19−27.

[24] KONOBEYEV A Y, FISCHER U, KOROVIN Y A, SIMAKOV S P. Evaluation of effective threshold displacement energies and other data required for the calculation of advanced atomic displacement cross-sections [J]. Nuclear Energy and Technology, 2017, 3(3): 169−175.

[25] PEDRAZA D F. Mechanisms of the electron irradiation-induced amorphous transition in intermetallic compounds [J]. Journal of Materials Research, 1986, 1: 425−441.
[26] QIN Wen, SZPUNAR J A, UMAKOSHI Y. Electron or ion irradiation-induced phase-change mechanism between amorphous and crystalline state [J]. Acta Materialia, 2011, 59(5): 2221−2228.
[27] DAI Z R, SUN S H, WANG Z L. Phase transformation, coalescence, and twinning of monodisperse FePt nanocrystals [J]. Nano Letters, 2001, 1(8): 443−447.
[28] COURTY A, HENRY A I, GOUBET N, PILENI M P. Large triangular single crystals formed by mild annealing of self-organized silver nanocrystals [J]. Nature Materials, 2007, 6: 900−907.
[29] LI Jun-jie, CHEN Jiang-chun, WANG Hua, CHEN Na, WANG Zhong-chang, GUO Lin, DEEPAK F L. In situ atomic-scale study of particle-mediated nucleation and growth in amorphous bismuth to nanocrystal phase transformation [J]. Advanced Science, 2018, 5(6): 1700992.
[30] ZOU Lian-feng, LI J, ZAKHAROV D, STACH E, ZHOU Guang-wen. In situ atomic-scale imaging of the metal/oxide interfacial transformation [J]. Nature Communications, 2017, 8: 307.
[31] LI Qi-kai, LI Mo. Atomistic simulations of correlations between volumetric change and shear softening in amorphous metals [J]. Physical Review B, 2007, 75(9): 094101.

γ 射线和电子辐照对 SnPb 共晶焊点显微组织演变和力学性能的影响

关旗龙[1]，杭春进[1,2]，张 威[1]，李胜利[1]，唐晓玖[1]，于 丹[3]，丁 颖[3]，王修利[3]，张玉宝[4]

1. 哈尔滨工业大学 材料结构精密焊接与连接全国重点实验室，哈尔滨 150006；
2. 哈尔滨工业大学 郑州研究院，郑州 450046；
3. 北京控制工程研究院，北京 100094；
4. 黑龙江省原子能研究院，哈尔滨 150086

摘 要：研究了 γ 射线和电子辐照对 SnPb 共晶焊点显微组织演变及力学性能的影响。经过电子辐照后，由 γ 射线辐照诱导的 SnO_2 相转化为 β-Sn，且 β-Sn 晶体中的位错密度降低。大量点缺陷团簇在 β-Sn 晶体中形成，部分转变为非晶相，且非晶层厚度增加。同时，电子辐照还引起 β-Sn 纳米晶(220)晶面的旋转和 SnO_2 的还原。此外，经 γ 射线和电子辐照后，焊球的平均剪切强度最初增加了 10.10%，随后分别降低了 3.53%和 4.77%。焊点塑性和断口表面的韧窝数量先降低后增加。

关键词：耦合辐照；SnPb 共晶焊点；SnO_2 还原；辐照损伤；β-Sn 纳米晶旋转

(Edited by Wei-ping CHEN)